7

Interpretation of Results

This chapter presents first attempt of the interpretation of the measured data. The obtained asymmetries, presented in section 6.8, will be confronted by the theoretical predictions of the Bochum/Krakow group. The comparison with the calculations will be done separately for all three reaction channels $^3\vec{\mathrm{He}}(\vec{e},e'\mathrm{d})\mathrm{p}$, $^3\vec{\mathrm{He}}(\vec{e},e'\mathrm{p})\mathrm{d}$ and $^3\vec{\mathrm{He}}(\vec{e},e'\mathrm{p})\mathrm{pn}$. A special attention wil be dedicated to the first two channels, which are experimentally under better control. The extraction and intepretation of the asymmetries for the latter channel is presently confined by an inaccurate separation of the three-body breakup from the two-body breakup channel. The comparison with the previous double-polarization asymmetry measurement from Mainz will also be performed. In the end, the conclusions will be drawn, together with a summery of remaining open problems and challanges for the future work.

7.1 The two-body breakup channel $^3\vec{\mathrm{He}}(\vec{e},e'\mathrm{p})\mathrm{d}$

The experimental asymmetries shown in Figs. 6.31 to 6.33, where proton is detected by the BigBite are hybrids, combined of the asymmetries for the reactions $^3\vec{\mathrm{He}}(\vec{e},e'\mathrm{p})\mathrm{d}$ and $^3\vec{\mathrm{He}}(\vec{e},e'\mathrm{p})\mathrm{pn}$. The relative contribution of each reaction channel is governed by the cross-section ratio for the two processes. To isolate asymmetry corresponding to the reaction $^3\vec{\mathrm{He}}(\vec{e},e'\mathrm{p})\mathrm{d}$, the two-body breakup events (2BBU) must be separated from the three-body breakup events (3BBU).

This is accomplished by inspecting the missing energy histogram, where the 2BBU events generate a peak around $E_{\mathrm{Miss}} = 5.5\,\mathrm{MeV}$, while 3BBU events gather arround $E_{\mathrm{Miss}} = 7.7\,\mathrm{MeV}$. The obtained peaks are usually smeared by the radiative losses and limited resolutions of the spectrometers. The analysis has shown (see Fig. 7.1), that for our data these effects are soo large, that two-body breakup peak can no longer be distinguished from the the three-body peak. This represents an important obstacle in the interpretation of our results and requires a precise Monte-Carlo simulation of the experiment for proper description of the measured data and comparison with the theory.

Unfortunatelly a detailed simulation for this experiment is not yet available. Instead, an approximate empirical approach was considered for first approximate extraction of the 2BBU asymmetries. Obtained results are shown in Fig. 7.2. In this procedure measured $(e,e'\mathrm{p})$ asymmetries were plotted as a function of missing energy.

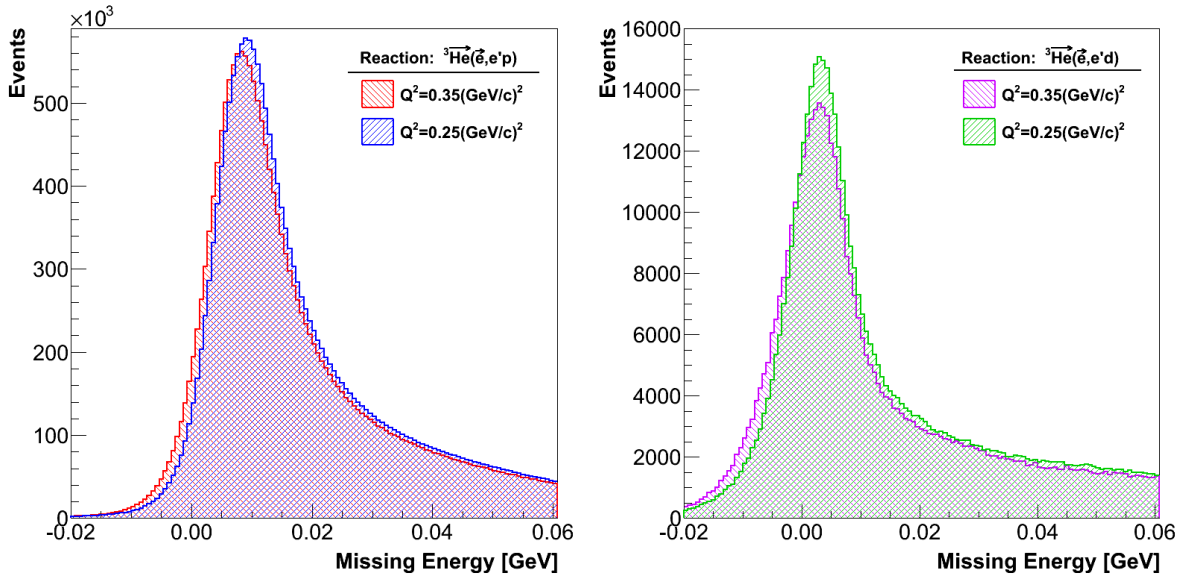

Figure 7.1 — The reconstructed distributions of missing energy E_{Miss} for reactions $^3\vec{He}(\vec{e}, e'p)$ (left) and $^3\vec{He}(\vec{e}, e'p)d$ and $^3\vec{He}(\vec{e}, e'd)p$ (right). Plots show results for both kinematical settings $Q^2 \approx 0.35,\ 0.25\,(GeV/c)^2$. Due to the radiative effects and poor spectrometer resolutions, the 2BBU and 3BBU peaks in the proton channel can not be distinguished.

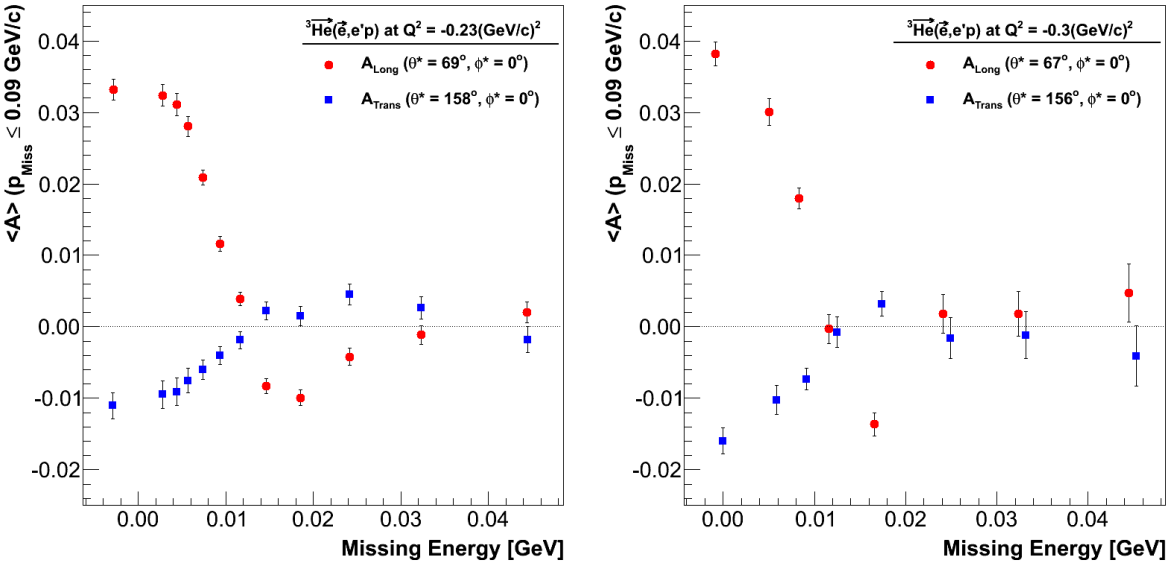

Figure 7.2 — Mean asymmetries, averaged over the missing momenta between $p_{Miss} = 0 - 90\,MeV/c$, shown as a function of missing energy E_{Miss}. Left and right plot show longitudinal and transverse asymmetries for kinematical settings $Q^2 = -0.23\,(GeV/c)^2$ and $Q^2 = -0.3\,(GeV/c)^2$ respectively.

Here only events with low missing momentum $p_{Miss} \leq 90\,MeV/c$ were acknowledged. In this limit is the ^{3}He-wave function dominated by the S-state, which encourages a large asymmetry in the case of the 2BBU and almost a zero asymmetry for the 3BBU (see Sec. **??** for more detail). The measured asymmetry agree well with this hypothesis. We obtain a large positive asymmetry in region of small E_{Miss} governed by the

2BBU, which then evetually resonates to zero, at large E_{Miss} , where 3BBU is expected to dominate. A negative asymmetry in the middle region $E_{Miss} \approx 15\,MeV$ is a result of interactions between nucleons. The Mainz experiment [31] has described this with the FSI, that generate a strong effect in the 3BBU channel at low E_{Miss}, which then weakens at higher E_{Miss}. This also explains a rapid fall of the asymmetry at $E_{Miss} \approx 6MeV$, where the 3BBU process starts to contribute.

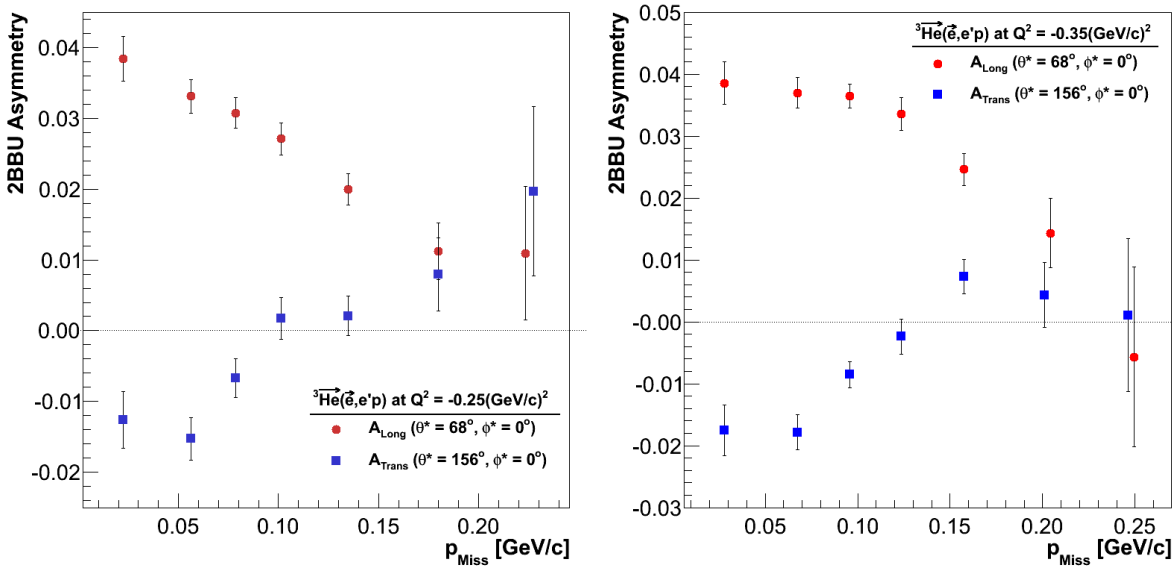

Figure 7.3 — The longitudinal and transverse $^3\vec{He}(\vec{e},e'p)d$ asymmetries for $Q^2 = -0.23\,(GeV/c)^2$ (left) and $Q^2 = -0.3\,(GeV/c)^2$ (right). The asymmetries were determined by selecting only expertimental with $E_{Miss} \leq 1.6\,MeV$.

An almost flat asymmetry at very low missing energies indicates a dominance of the 2BBU reaction for $E_{Miss} \lesssim 2\,MeV$. Relaying on this assumption, the 2BBU asymmetries were extracted from the complete set of measuremnts, by selecting only events with $E_{Miss} \leq 1.6\,MeV$. Both longitudinal and transverse asymmetries were obtained. Results for both kinematical settings are gathered in Fig. 7.3.

The determined approximate 2BBU asymmetries are ready to be challanged by the theoretical predictions. The calculations were performed by the Bochum/Krakow group [**?**]. They were able to peform calculation of asymmetries for eleven different kinematics points, whiha are gathered in Table 7.1 and shown in Fig. 7.4. Since they are confortable performing calculations only for $Q^2 \lesssim 0.3\,(GeV/c)^2$, points were selected to cover the whole kinematical acceptance, for setting when HRS-L is positioned at scattering angle of $\theta_{HRS-L} = 12.5°$. In a section with highest statistics, selected bin was divided even further into three smaller bins. Kinematical points for $Q^2 > 0.3\,(GeV/c)^2$, that are accessible when HRS-L positioned at $\theta_{HRS-L} = 14.5°$ were not yet calculated. The theory will therefore be tested mostly with the $Q^2 = -0.25\,(GeV/c)^2$ data. However, since the two kinematical settings overlap in the middle region arround $Q^2 = -0.3\,(GeV/c)^2$, some checks could also be performed with the data, that were taken with $HRS-L$ at $\theta_{HRS-L} = 14.5°$.

Beside the data used to fixate the electron kinematics and properly orient the target (θ^*, ϕ^*), the calculations require as an input also momentum of detected proton $\tilde{p}$ and the polar angle θ_p between the momentum trasfer vector $\vec{q}$ and proton momentum $\vec{p}$

Table 7.1 — The list of eleven kinematic points considered in the theoretical calculations. The points are selected to cover the whole kinematical acceptance when HRS-L is positioned at in-plane scattering angle $\theta_{HRS-L} = 12.5°$. The section with highest statistics was further divided into three smaller bins. The Bochum/Krakow group is able to predict asymmetries for each of the points separately. The size of the momentum transfer vector q for each combination of E, E' and θ_e stated in the table was obtaied by using Mainz kinemtic calculator [116].

Kinematic Points for Theory

i	E [MeV]	E′ [MeV]	θ_e [deg]	q [MeV/c]	ω [MeV]
1	2425.5	2.235	11.35	498.2	190.5
2	2425.5	2.268	11.35	488.0	157.5
3	2425.5	2.285	11.35	485.0	140.5
4	2425.5	2.302	11.35	485.0	123.5
5	2425.5	2.335	11.35	480.0	90.5
6	2425.5	2.235	12.45	538.7	190.5
7	2425.5	2.285	12.45	526.9	140.5
8	2425.5	2.335	12.45	519.8	90.5
9	2425.5	2.235	13.55	579.8	190.5
10	2425.5	2.285	13.55	570.7	140.5
11	2425.5	2.335	13.55	567.7	90.5

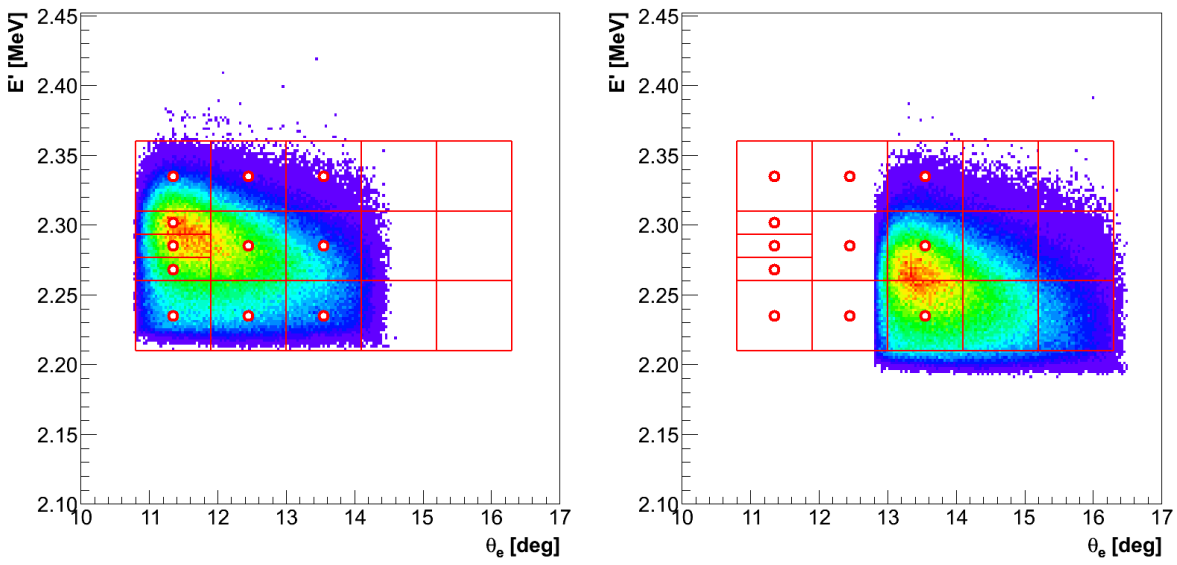

Figure 7.4 — The electron kinematics accesible during the E05-102 experiment. Left and right plots show results when HRS-L was positioned at $\theta_{HRS-L} = 12.5°$ and 14.5°, respectively. The whole kinematical coverage was divided into 17 sections. Theoretical calculations were performed for the centers of first 11 bins (demonstrated with circles).

(see Fig. **??**) for each selected bin in missing momentum p_{Miss}. Considering the conservation of energy and momentum in the non-relativistic limit, the θ_p is used to calculate

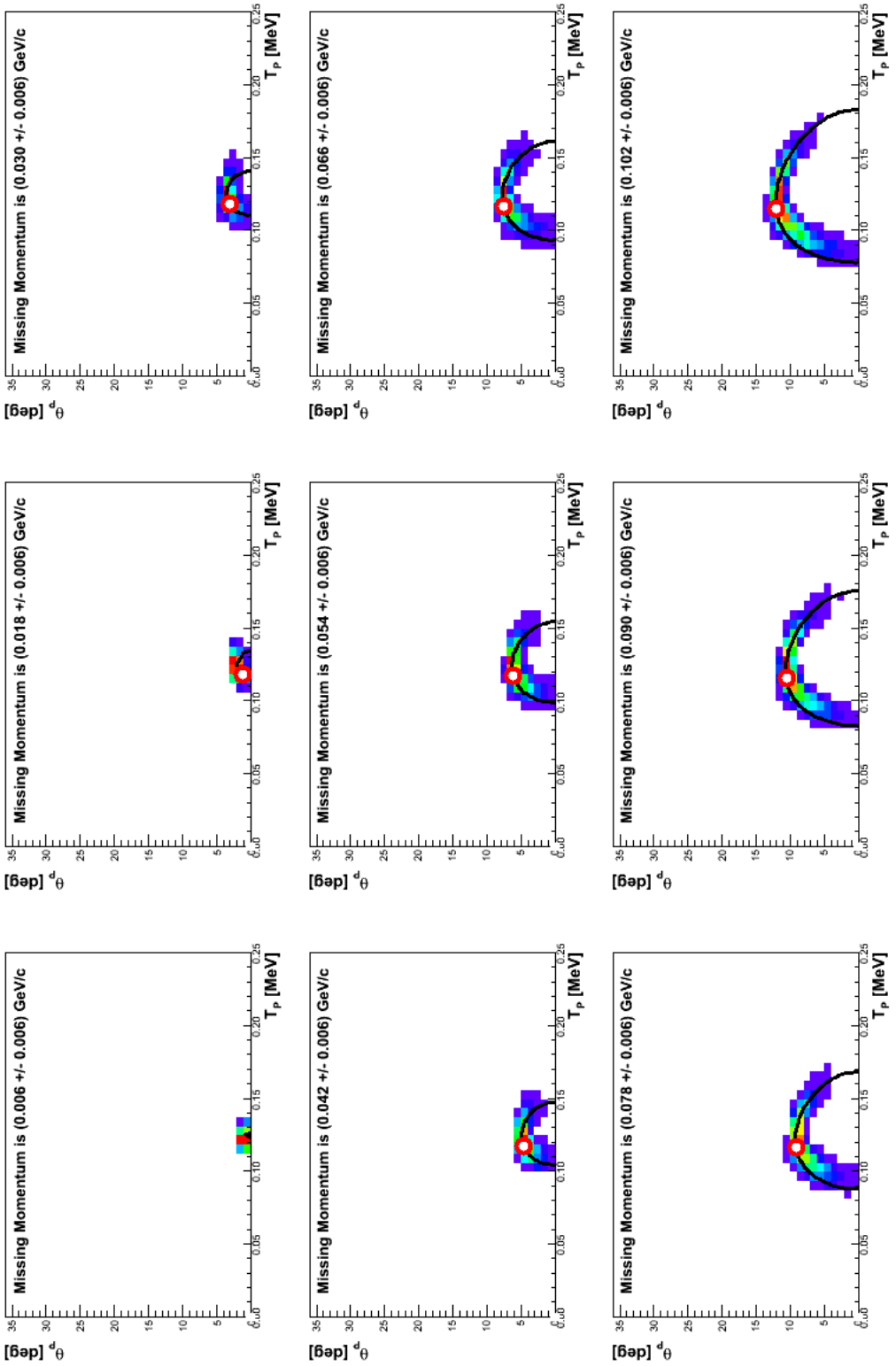

Figure 7.5 — The two dimensional histograms showing the relation between prot5on angle θ_p and its kinetic energy $T_p \approx p^2/2M_p$ for each of the selected bins in p_{Miss}. For these plots only section of data, surrounding the 4^{th} kinematics point, were considered (see Fig. 7.4). The lengths of obtained bands are controlled by the remaining spread in ω and $\vec{q}$. Black lines show solutions of Eq.(7.2) for a given p_{Miss} and $|\vec{q}| = 485.0\,MeV/c$. Circles show $(\theta_p, \tilde{p})$ pairs considered in the theoretical calculations. For a selected kinematic point, the events with very low missing momenta are not permited. Hence, theoretical point is missing in the histogram for $p_{Miss} = 6\,MeV$.

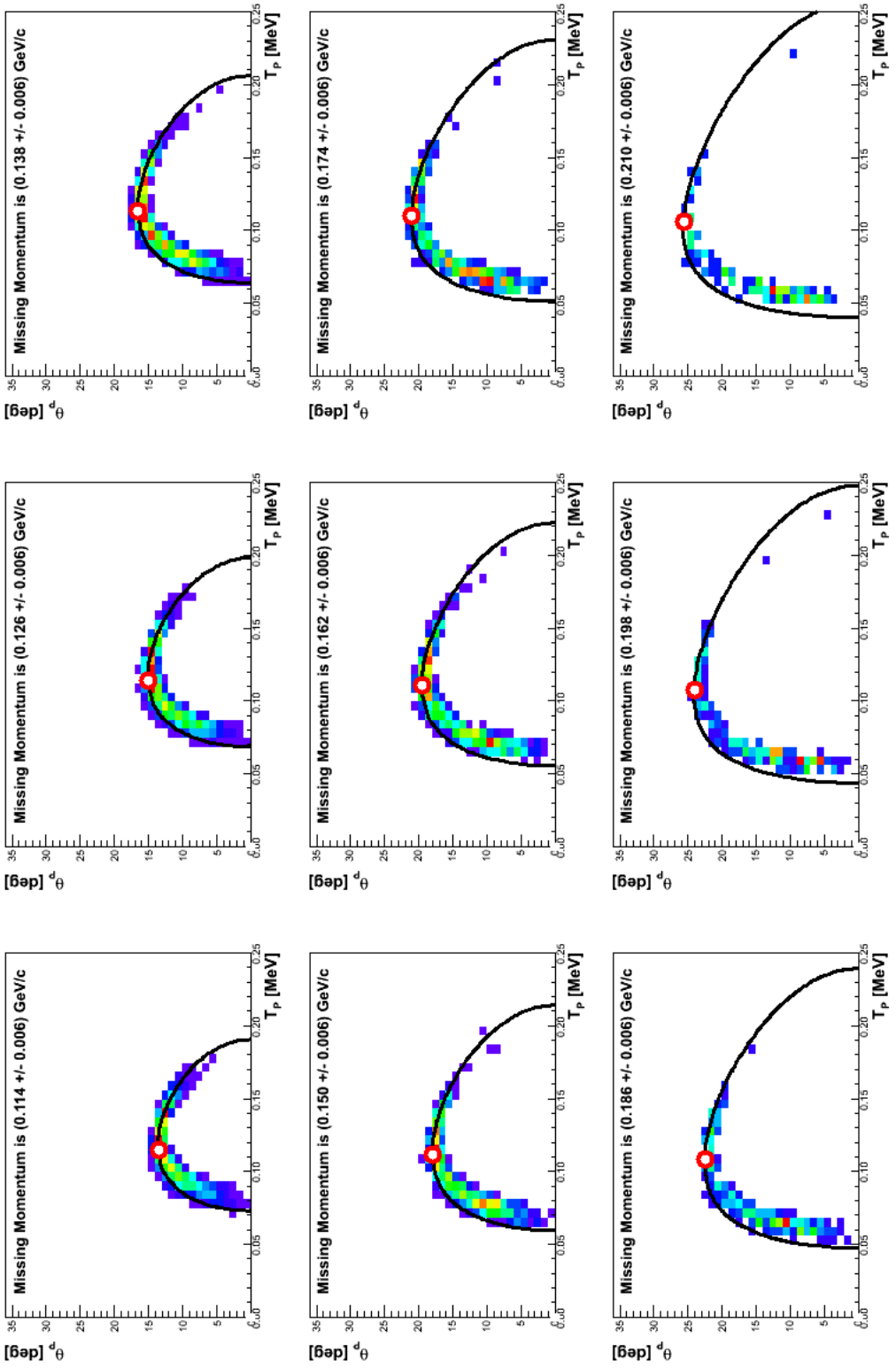

Figure 7.6 — The two dimensional histograms showing the relation between prot5on angle θ_p and its kinetic energy $T_p \approx p^2/2M_p$ for each of the selected bins in p_{Miss}. For these plots only section of data, surrounding the 4^{th} kinematics point, were considered (see Fig. 7.4). The lengths of obtained bands are controlled by the remaining spread in ω and $\vec{q}$. Black lines show solutions of Eq.(7.2) for a given p_{Miss} and $|\vec{q}| = 485.0\,MeV/c$. Circles show $(\theta_p, \tilde{p})$ pairs considered in the theoretical calculations.

the momentum of the detected proton p, independently of the input parameter $\tilde{p}$:

$$\text{Conservation of Energy :} \quad \omega + M_{^3\text{He}} = M_p + M_{\text{Miss}} + \frac{\vec{p}^2}{2M_p} + \frac{\vec{p}_{\text{Miss}^2}}{2M_{\text{Miss}}}, \quad (7.1)$$

$$\text{Conservation of Momentum :} \quad \vec{p}^2_{\text{Miss}} = \vec{q}^2 + \vec{p}^2 - 2|\vec{p}|\,|\vec{q}|\cos\theta_p\,. \quad (7.2)$$

Here, p_{Miss} and M_{Miss} are the momentum and mass of the undetected deuteron. Inserting Eq.(7.2) into Eq.(7.1), a quadratic equation for the proton momentum p is obtained:

$$p = \frac{(2M_p q\cos\theta_{pq}) \pm \sqrt{(2M_p q\cos\theta_{pq})^2 - 4(M_p + M_{\text{Miss}})(M_p q^2 - 2M_p M_{\text{Miss}} - H)}}{2(M_p + M_{\text{Miss}})},$$

where $H = \omega + M_{^3\text{He}} - M_p - M_{\text{Miss}}$. Equation has two solutions, and algorithm chooses the closest to the $\tilde{p}$. This way the input parameter $\tilde{p}$ serves only for selecting the physical solution of the equation. This kinematical walk arround is utilized as an protection mechanism before any non-physical input combinations of $\tilde{p}$ and the polar angle θ_p.

In the analysis, the correct pairs $(\theta_p, \tilde{p})$ for each p_{Miss} bin were obtained from the corresponding two-dimensional histograms. Here, only data located within a square box arround the selected kinematics point (see Fig. 7.4) were considered . The obtained distributions for the 4^{th} kinematical bin are demostrated in Figs. 7.5 and 7.5. In spite of the tight kinematical cuts, the accepted events still have some freeedom in ω and $\vec{q}$. Consequently, data for each p_{Miss} bin are not gathered in a single point, but form a band. The shape of the band is dictated by the Eq. 7.2, while its length is governed by the spread in $omega$ and $\vec{q}$. The pairs $(\theta_p, \tilde{p})$ conidered in the calculations are marked with circles, and represent points, where all the data would be gathered, if the chosen kinematical region would be reduced to an infinitizimally small section of data around the chosen kinematical point. Unfortunatelly such narrow cuts not be performed on data, because then all the statistics would be lost.

Once the input data was available, the theoreticians could perform calculations for all eleven kinematic points. For each target orientation and each bin in missing momentum, they generated asymmetry as a function of the angle ϕ_p (see Fig. **??**). The calculated longitudinal and transverse asymmetry for the 4^{th} kinmeatic point are shown in Figs. 7.7 and 7.8, respectively.

The experimental results are not separated in terms of bins in ϕ_p. The theoretical calculations must therefore be averaged over the angle ϕ_p in order to be able to compared them to the measured asymmetries. This procedure is not trivial, since the ϕ_p distribution depends strongly on both, selected kinematical point and p_{Miss}. Fig. 7.9 shows the ϕ_p distribution for various p_{Miss}, obtained for 4^{th} kinematic point. In the region of low missing momenta, angles around $\phi_p \approx 180^\circ$ dominate. However, when moving towards the higher missing momenta, the events with $phi_p \approx 90^\circ, 270^\circ$ become superior . Since the theoretical asymmetries for $p_{\text{Miss}} \geq 100\,\text{MeV/c}$ have a strong angular dependence, is a proper averaging over the ϕ_q crucial for correct interpretation of the calculations.

The appropriate averaging of the calculated asymmetries was achieved by generating the ϕ_p histograms for each p_{Miss} in all eleven kinematic regions. The obtained distributions were then considered as weights in the weighted average formula, that

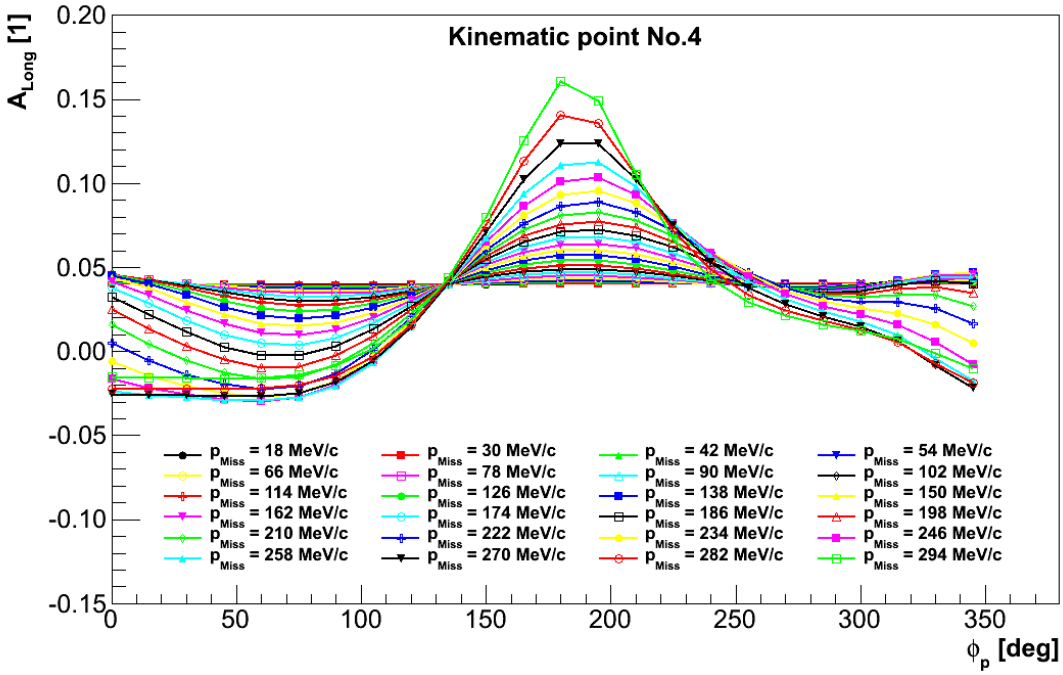

Figure 7.7 — The theoretical predictions for the longitudinal $^3\vec{\mathrm{He}}(\vec{e}, e'p)d$ asymmetry $A_{\mathrm{Long}} = A(\theta^* = 68°, \phi^* = 0°)$ as a function of an angle ϕ_p between reaction and scattering plane, for missing momenta $p_{\mathrm{Miss}} \leq 300\,\mathrm{MeV}$. Presented asymmetries correspond to the results for the kinematics bin No. 4. Calculations were provided by the Bochum/Krakow group [**?**].

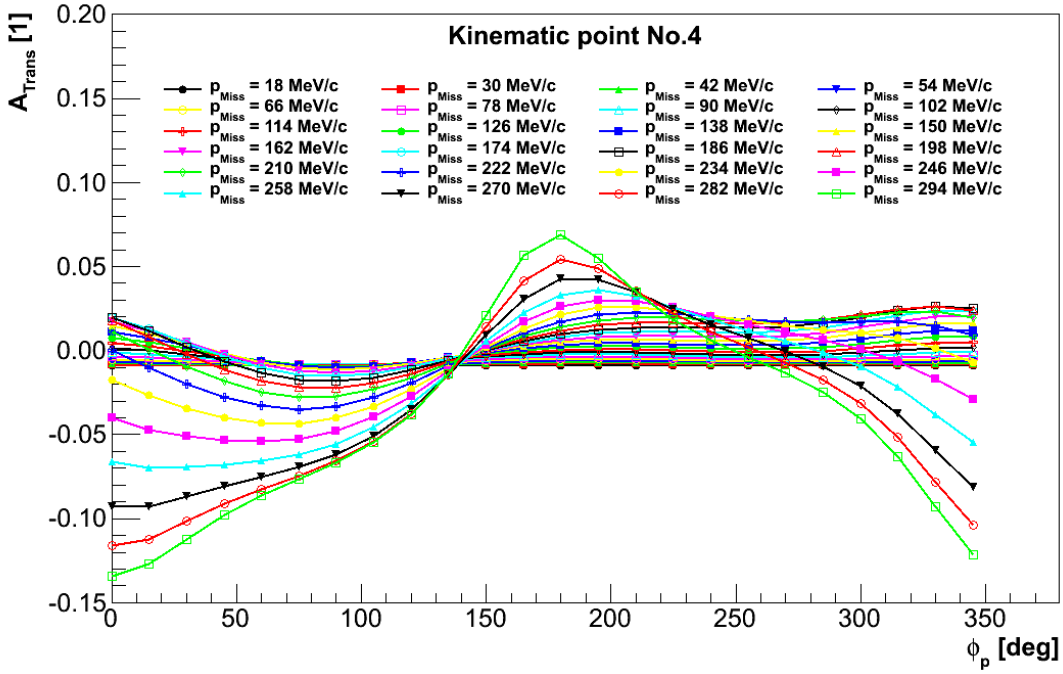

Figure 7.8 — The theoretical predictions for the transverse $^3\vec{\mathrm{He}}(\vec{e}, e'p)d$ asymmetry $A_{\mathrm{Trans}} = A(\theta^* = 156°, \phi^* = 0°)$ as a function of an angle ϕ_p between reaction and scattering plane, for missing momenta $p_{\mathrm{Miss}} \leq 300\,\mathrm{MeV}$. Presented asymmetries correspond to the results for the kinematics bin No. 4. Calculations were provided by the Bochum/Krakow group [**?**].

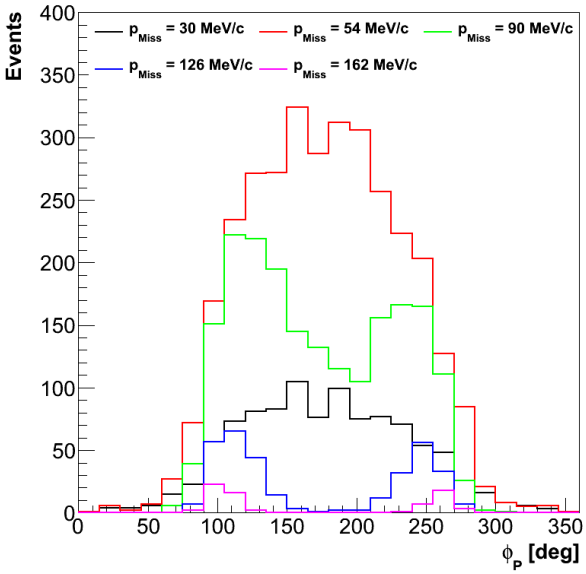

Figure 7.9 — The distributions of ϕ_p at different p_{Miss}, determined for the events gathered around the 4^{th} kinematic point. At low missing momenta, the angles aroung $\phi_p = 180°$ dominate, while at high missing momenta, events with $\phi_p \approx 90°, 270°$ prevail.

was utilized for averaging of the asymmetries:

$$\overline{A}(p_{Miss}) = \frac{\sum_{\phi_p^i} A(p_{Miss}, \phi_p^i) N_{\phi_p^i}}{\sum_{\phi_p^i} N_{\phi_p^i}},$$

where ϕ_p^i goes over all bins in the $\phi_p(p_{Miss})$ distribution and $N_{\phi_p^i}$ represents the number of events in each of the bins. $A(p_{Miss}, \phi_p^i)$ represent calculated asymmetries shown in Figs. 7.7 and 7.8, while $\overline{A}(p_{Miss})$ is the resulting average asymmetry for a particular p_{Miss}.

After the average asymmetries were calculated for all p_{Miss} available for a selected kinematic point, they could be compared to the theory. Separate comparisons were done for each kinematic points. Such comparisons are only approximate since each of the eleven calculated asymmetry describes only one section of data, while the experimental asymmetries represent an average over whole acceptance. For a rigorous comparison, further averaging needs to be perfored over whole kinematical acceptance, combining the theoretical asymmetries of all eleven kinematic points. This requires an understanding of the asymmetry behavior in the region inbetween two calculated points. The interpolation of the calculated asymmetries to the whole kinematic acceptance has not been addressed yet and represents one of the challanges for the future work.

In spite of these open problems, the comparison of the predictions for individual kinematic points to the data already provides us with some important findings. Fig. 7.10 shows the comparison of the data to the calculations for the most populated kinematical point No. 4. It is also the only point, which can provide information on the asymmetries at low missing momenta. For all other kinematic points provide information only for higher missing momenta. The calculated asymmetry seems to agree well with the measurements in the low missing momentum region. The theoretical calculations and measured data behave similarly also at higher missing momenta. However, the experimtal asymmetry A_{Long} seems to be descreasing much faster to zero than the calculated one. The inspection of the rest of the calculations has shown, that predicted

asymmetry in all the kinematical bins remains at $A_{Long}^{Calc.} \approx 0.04$, or even increase to higher values. Some examples are shown in Figs. **??**. This means, that exprimental asymmetries at high missing momnta could not be properly described by this theory, even with the proper averaging of the calculations over the whole acceptance. Identical problems appear also when the calculations for 9th, 10th and 11th kinematic point were confronted with the $Q^2 = -0.35\,(GeV/c)^2$ measurements. Results are shown in Fig. **??** Finding the reason for this persisting discrepancy between the data and the theory therefore presents another dare that needs to be resolved in the future.

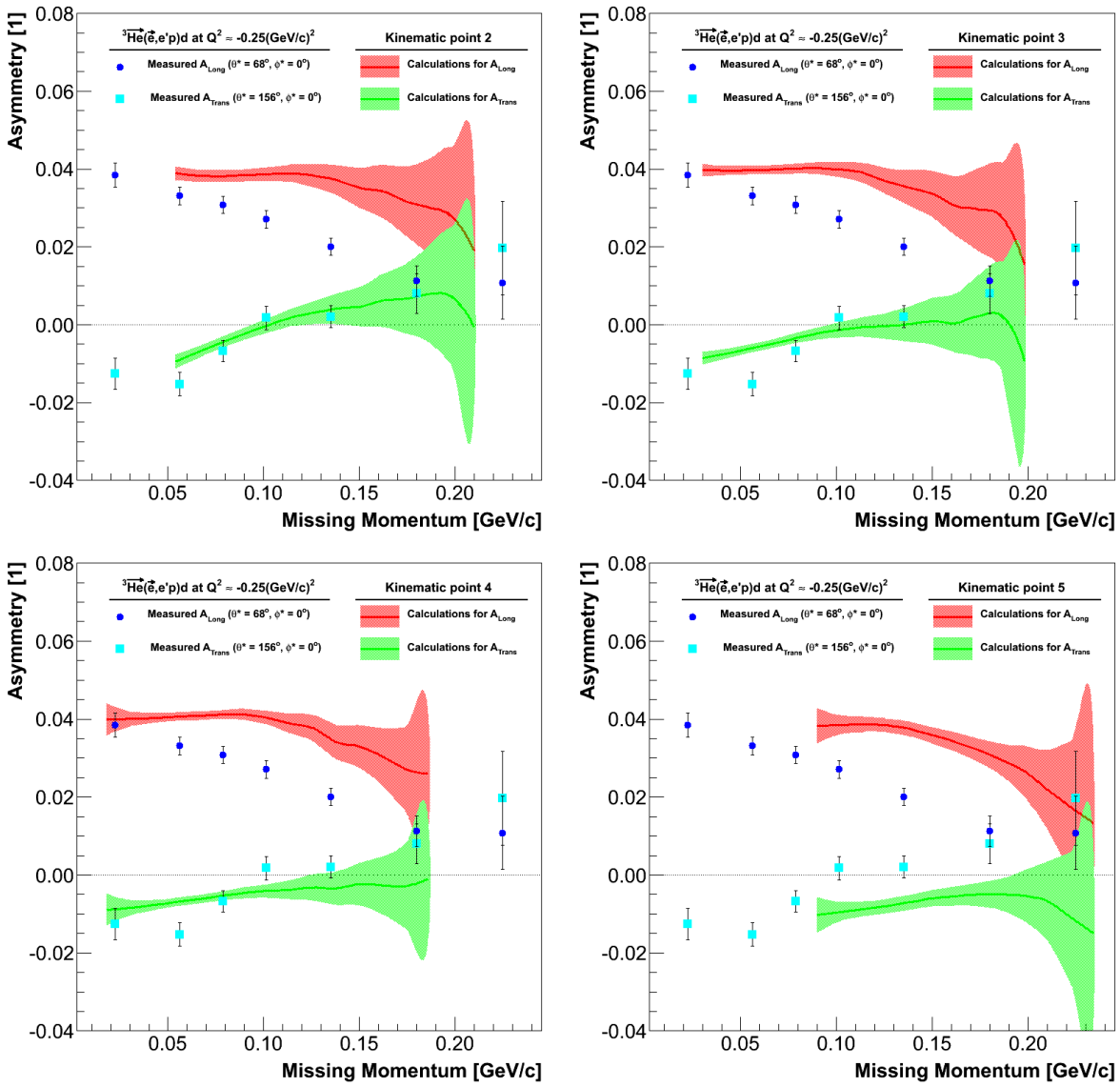

Figure 7.10 —

7.2 Relation to elastic scattering on $\vec{p}$

In a very simple picture, the ^{3}He ground-state can be imagined as a bound state of a deuteron and a proton. In this case the spin-part of the ^{3}He wave-function can be

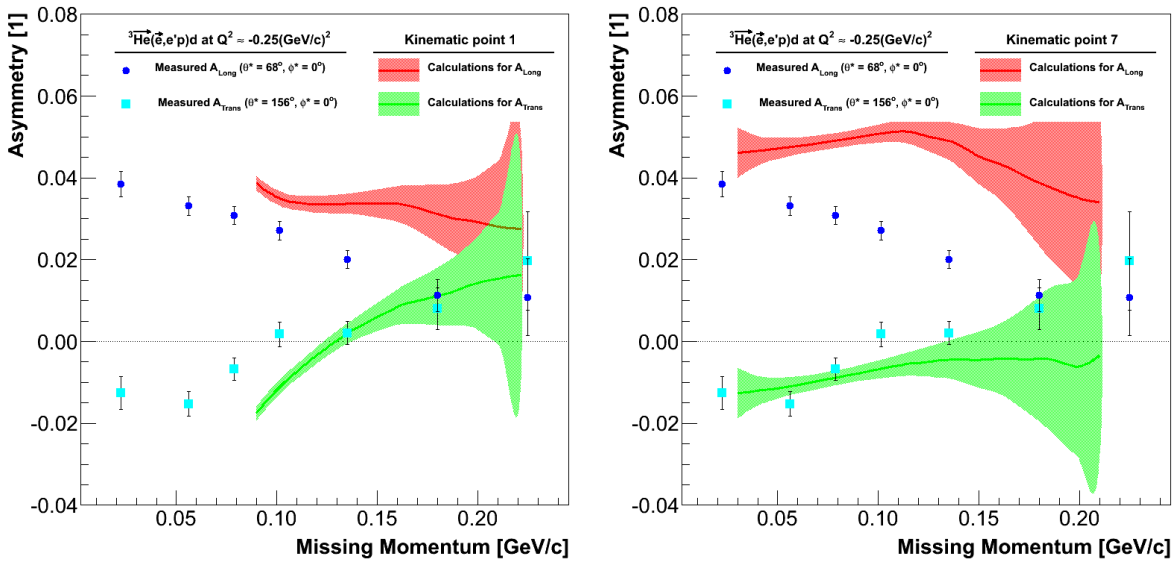

Figure 7.11 —

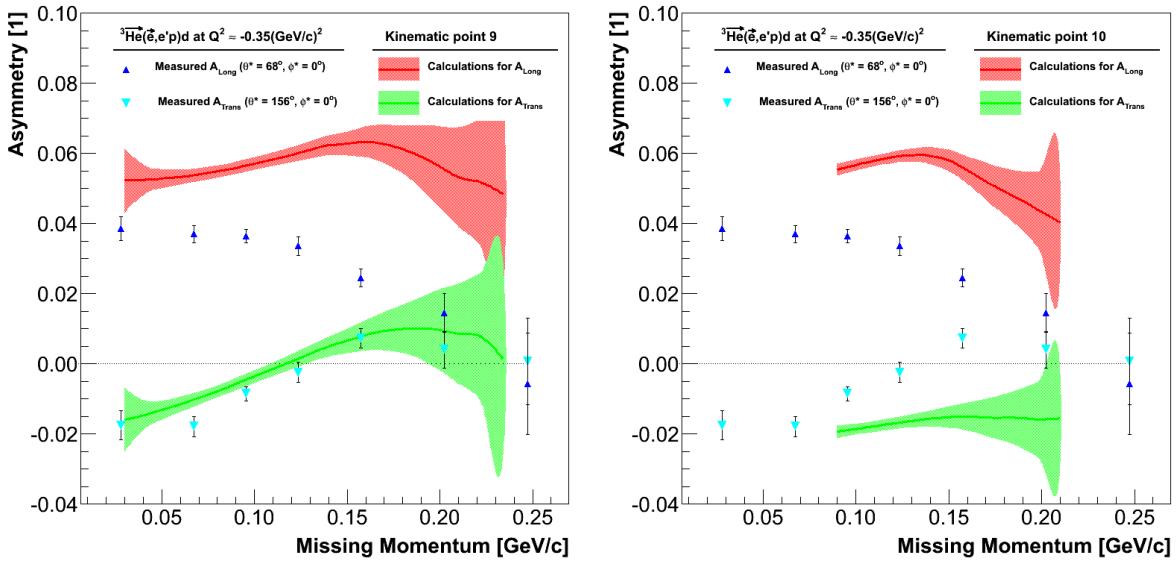

Figure 7.12 —

expressed in terms of Clebsh-Gordan coeficients as:

$$
\begin{aligned}
|J = 1/2, m_J = 1/2\rangle_{^3He} &= \sqrt{\frac{2}{3}}\,|J = 1, m_J = 1\rangle_d\,|J = 1/2, m_J = -1/2\rangle_p \\
&- \sqrt{\frac{1}{3}}\,|J = 1, m_J = 0\rangle_d\,|J = 1/2, m_J = 1/2\rangle_p\ , \qquad (7.3)
\end{aligned}
$$

where J and m_J represent the spin of a particle and the size of its third compponent, respectively. The expression (7.3) can now be utilized to estimate the polarization of the unbound proton inside the nucleus. When the ^{3}He nucleus is polarized along the

z-axis, the proton polarization P_p can be written as:

$$P_p = {}^{3}\mathrm{He}\langle 1/2,1/2|\ 2\,\hat{\sigma}_z^p\ P_{^3\mathrm{He}}\ |1/2,1/2\rangle_{^3\mathrm{He}} = P_{^3\mathrm{He}}\left[\frac{2}{3}\left(-\frac{2}{2}\right)+\frac{1}{3}\left(\frac{2}{2}\right)\right] = -\frac{1}{3}P_{^3\mathrm{He}}\,,$$

where $P_{^3\mathrm{He}}$ is the effective polarization of the helium, and $\hat{\sigma}_z^p$ is the Pauli matrix, considered for projecting proton spin to the z-axis. When ^{3}He is 100 % polarized, the proton polarization is $P_p \approx -33.3\,\%$. The negative sign of polarization means, that proton spin is predominantly oriented in the direction opposite to the nuclear spin.

This naive model of the ^{3}He can be further used to approximately describe the two-body electrodisintigration process $^3\vec{\mathrm{He}}(\vec{e},e'p)d$ at low missing momenta. In this limit, the virtual photon interacts only with a proton, while leaving the deuteron as a spectator at rest (see Sec. **??**). By neglecting any ineraction between proton and deuteron, this process can be simpifiled to the elastic scattering of electrons on polarized proton target $\vec{p}(\vec{e},e'p)$. This means, that the extracted $^3\vec{\mathrm{He}}(\vec{e},e'p)d$ asymmetries at $p_{\mathrm{Miss}} \approx 0$, should agree with the elastic proton asymmetry $A_{\vec{e}\vec{p}}$, corrected for the effective proton polarizatiom inside the ^{3}He:

$$A_{2\mathrm{BBU}}(p_{\mathrm{Miss}}=0,\theta^*,\phi^*) \approx -\frac{1}{3}A_{\vec{e}\vec{p}}(\theta^*,\phi^*)\,. \tag{7.4}$$

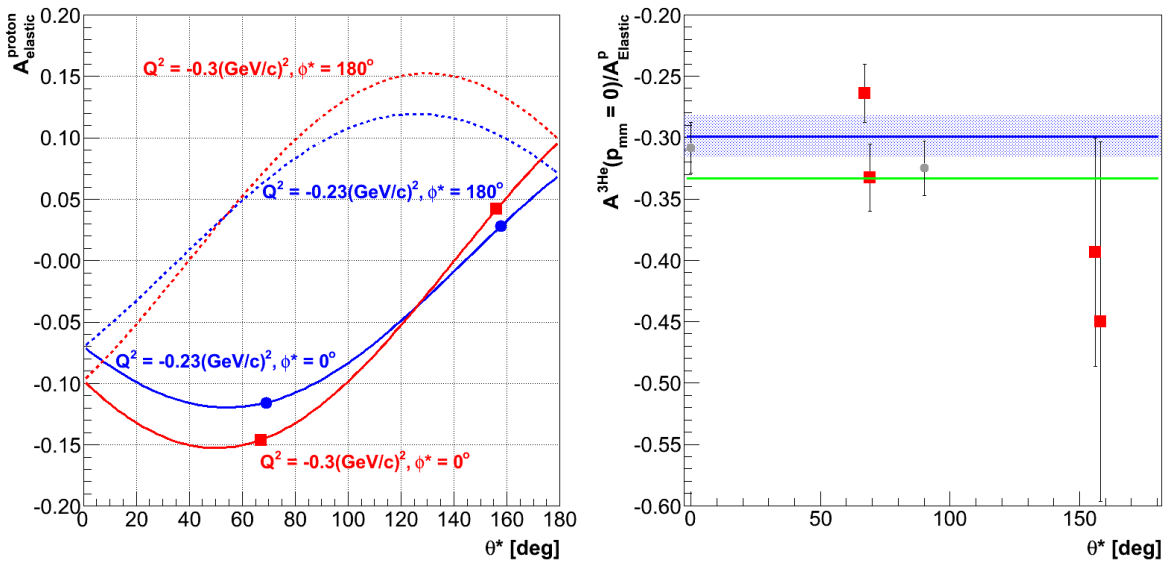

Figure 7.13 —

To test this hypothesis, the asymmetry ratios $A_{2\mathrm{BBU}}/A_{\vec{e}\vec{p}}$ were calculated for four data points closest to the $p_{\mathrm{Miss}} = 0$ (see Fig. 7.2). The elastic asymmetries corresponding to the selected datapoints were calculated using Eq. (**??**), and are shown in Fig. 7.13 (left). Determined ratios are presented in Fig. 7.13 (right). Results are nicely gathered around the predicted value (green line). By calculating the average value of four data points (blue line), the effective polarization of the proton was estimated to be:

$$\langle P_p \rangle = -0.299 \pm 0.0173\,,$$

which agrees well with value predicted in Eq. (7.4). This speeks in favor of the devised toy model and indicates that behaviour of the $^3\vec{\mathrm{He}}(\vec{e},e'p)d$ asymmetries at low missing momenta are understood.

7.3 The three-body breakup channel $^3\vec{\mathrm{He}}(\vec{e}, e'p)pn$

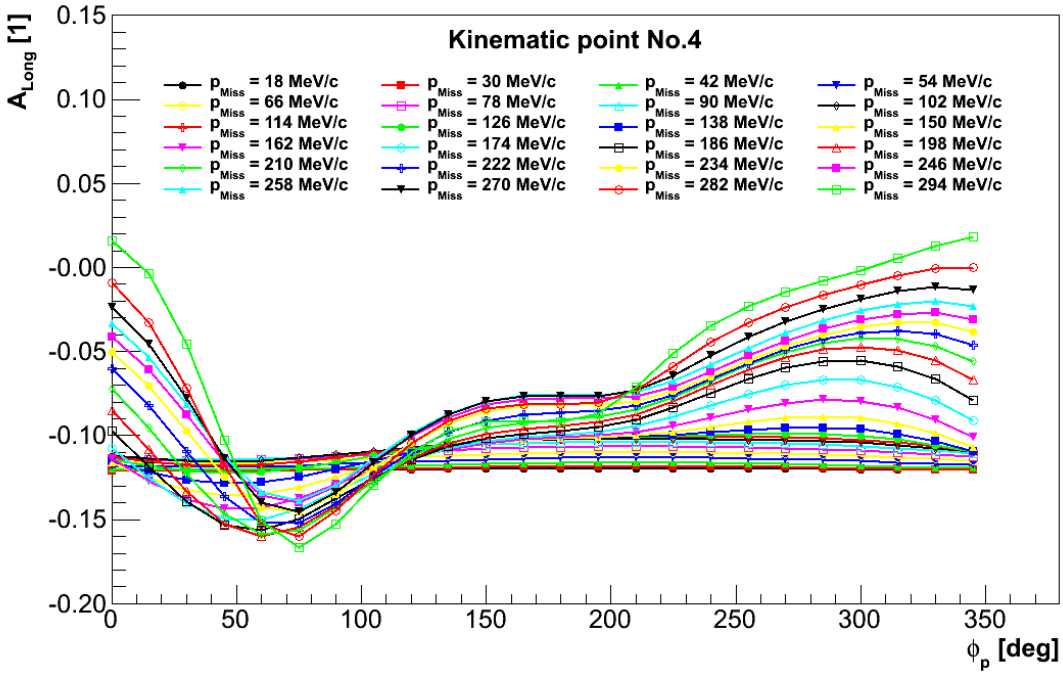

Figure 7.14 — The theoretical predictions for the longitudinal $^3\vec{\mathrm{He}}(\vec{e}, e'p)pn$ asymmetry $A_{Long} = A(\theta^* = 68°, \phi^* = 0°)$ as a function of an angle ϕ_p between reaction and scattering plane, for missing momenta $p_{Miss} \leq 300$ MeV. Presented asymmetries correspond to the results for the kinematics bin No. 4. Calculations were provided by the Bochum/Krakow group [**?**].

As already disscussed in Sec. At the moment only MCEEP is available.

7.4 Relation to previous results

7.5 The deuteron channel $^3\vec{\mathrm{He}}(\vec{e}, e'd)p$

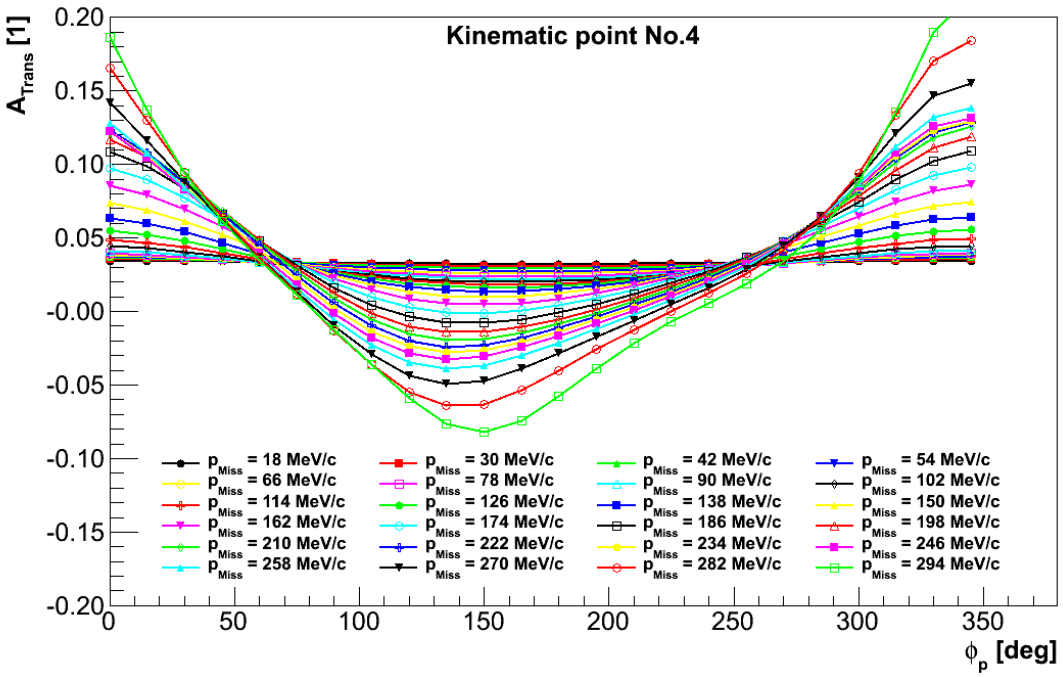

Figure 7.15 — The theoretical predictions for the transverse $^3\vec{\mathrm{He}}(\vec{e}, e'p)pn$ asymmetry $A_{\mathrm{Trans}} = A(\theta^* = 156°, \phi^* = 0°)$ as a function of an angle ϕ_p between reaction and scattering plane, for missing momenta $p_{\mathrm{Miss}} \leq 300\,\mathrm{MeV}$. Presented asymmetries correspond to the results for the kinematics bin No. 4. Calculations were provided by the Bochum/Krakow group [**?**].

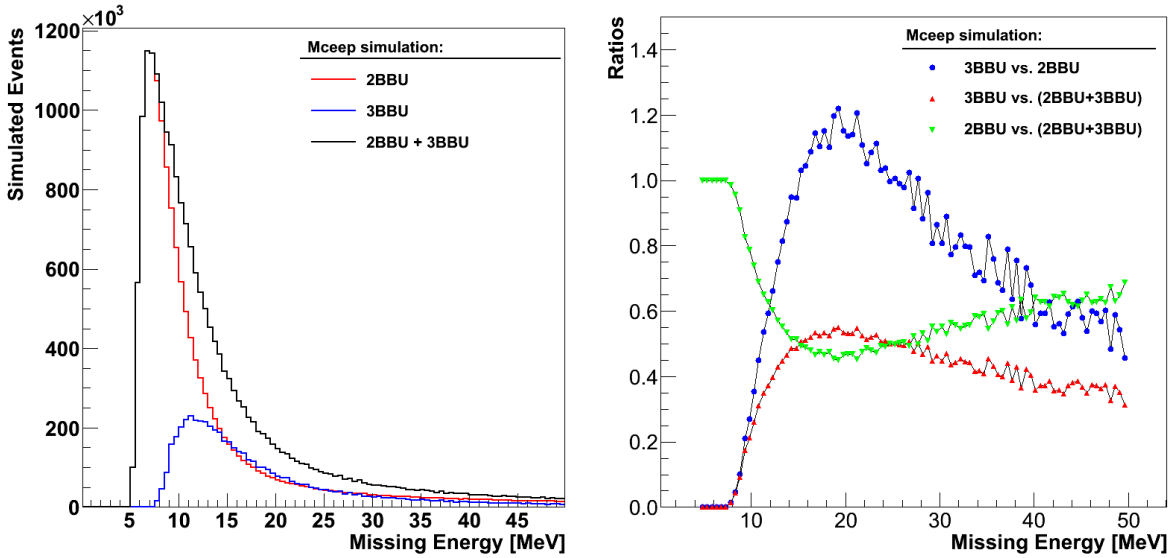

Figure 7.16 —

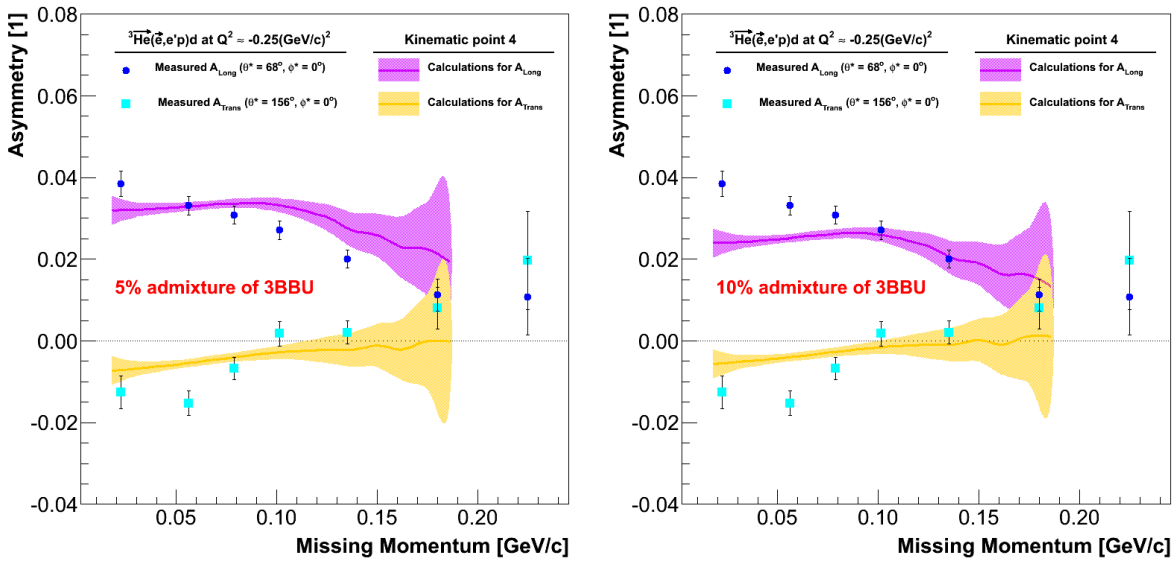

Figure 7.17 —

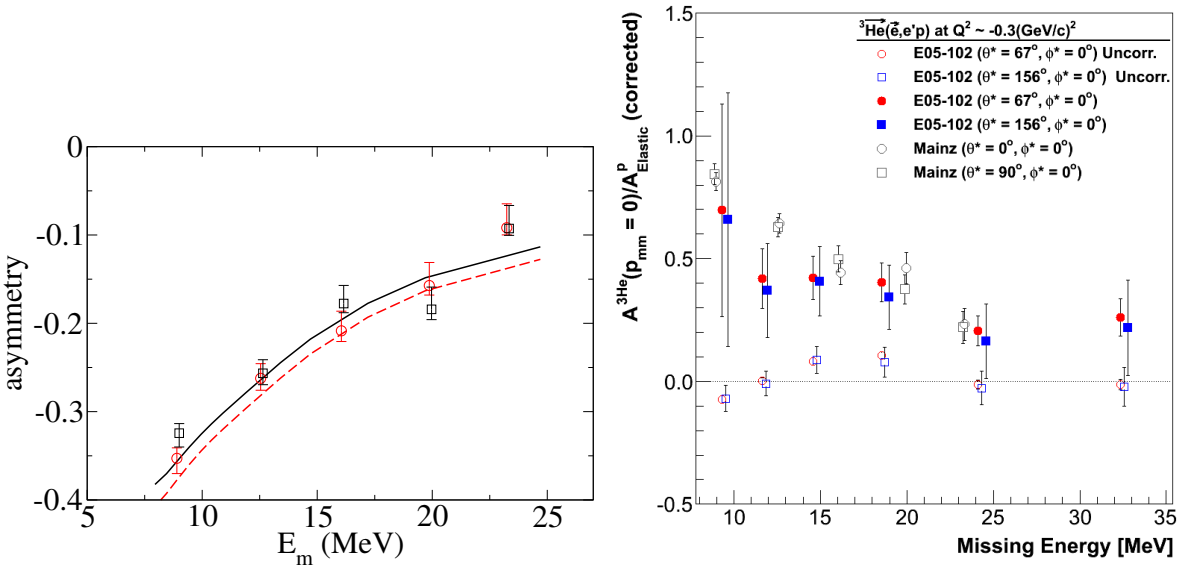

Figure 7.18 —

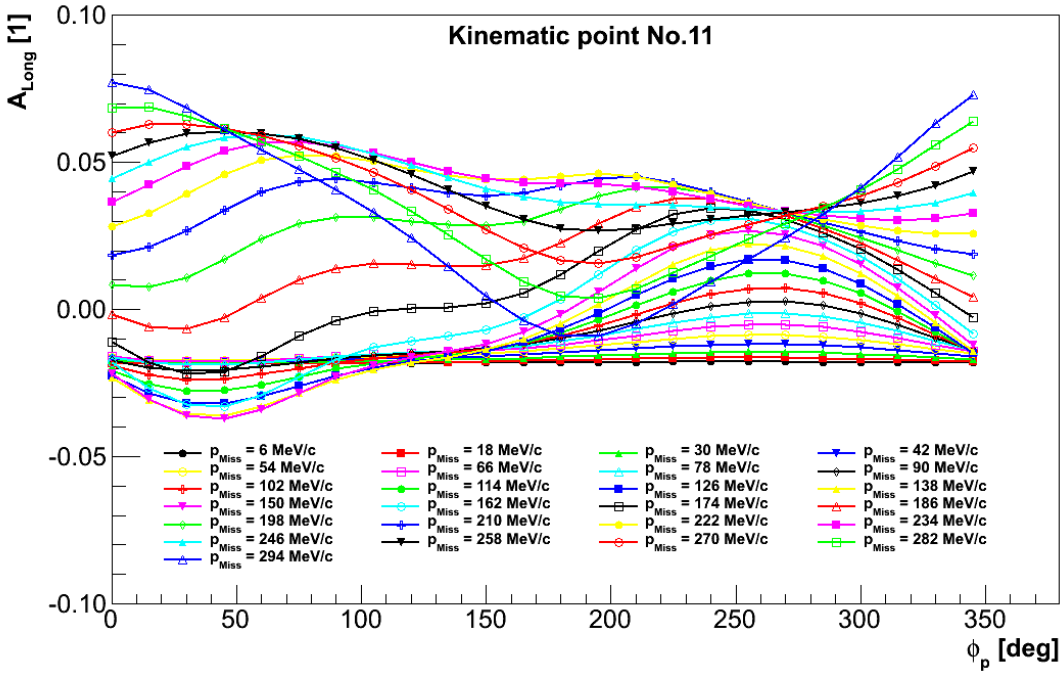

Figure 7.19 — The theoretical predictions for the longitudinal $^3\vec{\mathrm{He}}(\vec{e}, e'\mathrm{d})\mathrm{p}$ asymmetry $A_{\mathrm{Long}} = A(\theta^* = 73°, \phi^* = 0°)$ as a function of an angle ϕ_p between reaction and scattering plane, for missing momenta $p_{\mathrm{Miss}} \leq 300\,\mathrm{MeV}$. Presented asymmetries correspond to the results for the kinematics bin No. 11. Calculations were provided by the Bochum/Krakow group [**?**].

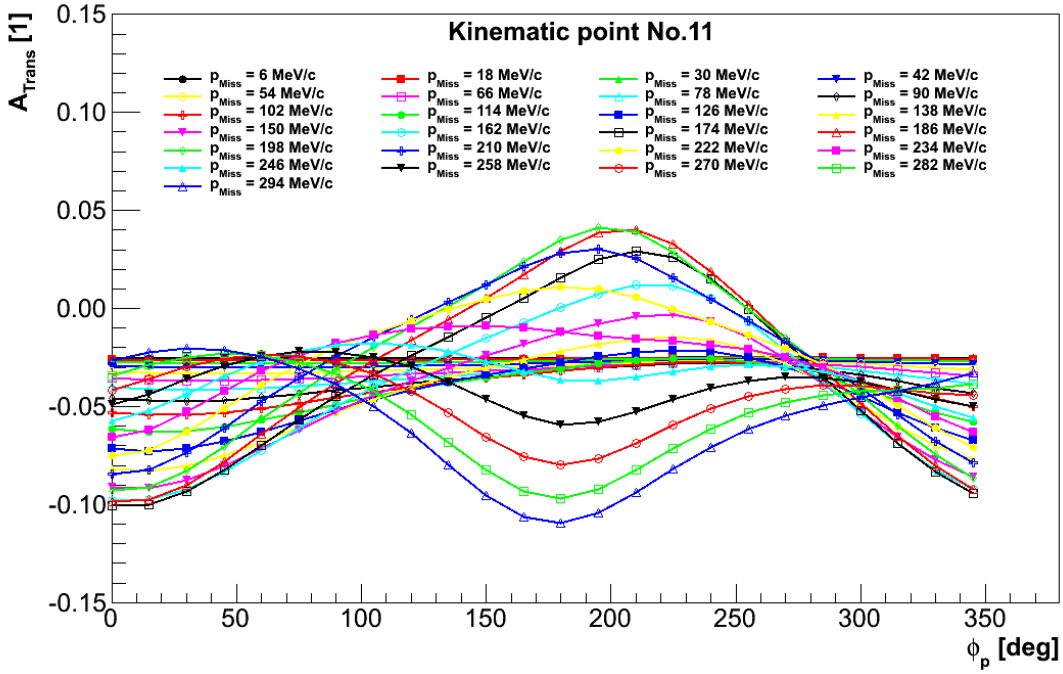

Figure 7.20 — The theoretical predictions for the transverse $^3\vec{\mathrm{He}}(\vec{e}, e'\mathrm{d})\mathrm{p}$ asymmetry $A_{\mathrm{Trans}} = A(\theta^* = 163°, \phi^* = 0°)$ as a function of an angle ϕ_p between reaction and scattering plane, for missing momenta $p_{\mathrm{Miss}} \leq 300\,\mathrm{MeV}$. Presented asymmetries correspond to the results for the kinematics bin No. 11. Calculations were provided by the Bochum/Krakow group [**?**].